

Protein Bricks: 2D and 3D Bio-Nanostructures with Shape and Function on Demand

Jianjuan Jiang, Shaoqing Zhang, Zhigang Qian, Nan Qin, Wenwen Song, Long Sun, Zhitao Zhou, Zhifeng Shi, Liang Chen, Xinxin Li, Ying Mao, David L. Kaplan, Stephanie N. Gilbert Corder, Xinzhong Chen, Mengkun Liu, Fiorenzo G. Omenetto, Xiaoxia Xia,* and Tiger H. Tao*

Precise patterning of polymer-based biomaterials for functional bio-nanostructures has extensive applications including biosensing, tissue engineering, and regenerative medicine. Remarkable progress is made in both top-down (based on lithographic methods) and bottom-up (via self-assembly) approaches with natural and synthetic biopolymers. However, most methods only yield 2D and pseudo-3D structures with restricted geometries and functionalities. Here, it is reported that precise nanostructuring on genetically engineered spider silk by accurately directing ion and electron beam interactions with the protein's matrix at the nanoscale to create well-defined 2D bionanopatterns and further assemble 3D bionanoarchitectures with shape and function on demand, termed "Protein Bricks." The added control over protein sequence and molecular weight of recombinant spider silk via genetic engineering provides unprecedented lithographic resolution (approaching the molecular limit), sharpness, and biological functions compared to natural proteins. This approach provides a facile method for patterning and immobilizing functional molecules within nanoscopic, hierarchical protein structures, which sheds light on a wide range of biomedical applications such as structure-enhanced fluorescence and biomimetic microenvironments for controlling cell fate.

Numerous research efforts have been invested in the precise placement of biological components and the controlled construction of functional bio-nanostructures, which opens up significant opportunities in applications from biointerfaces,^[1] biosensing,^[2] tissue engineering,^[3] to regenerative medicine.^[4] This includes both bottom-up and top-down approaches such as DNA origami^[5–9] via self-assembly^[10,11] and lithography-based nanopatterning techniques (e.g., e-beam lithography, EBL,^[12–14] nanoimprinting lithography,^[15,16] soft lithography,^[17,18] dip-pen nanolithography,^[19] and laser machining^[20]), where most methods yield only 2D and pseudo-3D structures with restricted geometries and functions. The limitation is mainly exerted by the fundamental challenge of harmonizing the existing integrated circuit-oriented nanofabrication technologies with biological systems thereby alleviating the inherent mismatch between biological (soft-wet) and nonbiological (hard-dry) components. However, since

Dr. J. Jiang, Dr. N. Qin, L. Sun, Z. Zhou, Prof. X. Li, Prof. T. H. Tao
State Key Laboratory of Transducer Technology
Shanghai Institute of Microsystem and Information Technology
Chinese Academy of Sciences
Shanghai 200050, China
E-mail: tiger.tao@austin.utexas.edu
S. Zhang, Prof. T. H. Tao
Department of Mechanical Engineering
The University of Texas at Austin
Austin, TX 78712, USA
Prof. Z. Qian, W. Song, Prof. X. Xia
State Key Laboratory of Microbial Metabolism
School of Life Sciences and Biotechnology
Shanghai Jiao Tong University
Shanghai 200240, China
E-mail: xiaoxiaxia@sjtu.edu.cn
L. Sun, Z. Zhou, Prof. T. H. Tao
School of Graduate Study
University of Chinese Academy of Sciences
Beijing 100049, China

Dr. Z. Shi, Dr. L. Chen, Prof. Y. Mao
Department of Neurosurgery
Huashan Hospital of Fudan University
Wulumuqi Zhong Road 12, Shanghai 200040, China
Prof. X. Li, Prof. T. H. Tao
School of Physical Science and Technology
Shanghai Tech University
Shanghai 200031, China
Prof. D. L. Kaplan, Prof. F. G. Omenetto
Department of Biomedical Engineering
Tufts University
Medford, MA 02155, USA
Dr. S. N. Gilbert Corder, Dr. X. Chen, Prof. M. Liu
Department of Physics and Astronomy
Stony Brook University
Stony Brook, NY 11794, USA

DOI: 10.1002/adma.201705919

most biological molecules are fragile and only functional in aqueous environments, there are severe constraints on the integration of biomolecules into conventional fabrication technologies which are usually optimized for inorganic compounds. Meanwhile, biomedical applications dictate precise reconstructions of the complex biological microenvironment with demanding requirement of 3D geometries and nanometer-sized features. Innovations in both materials and manufacturing techniques have yet to be explored.

In this context, silk proteins originating from silkworms^[21–24] and spider silks^[25,26] provide “green” alternatives to synthetic materials with advantages such as superior mechanical properties (paramount for creating sophisticated 3D nanostructures without collapsing), outstanding biocompatibility, ease of functionalization, controllable water-solubility, and tunable degradation rate, all of which offer numerous opportunities for processing, biological adaptation, and integration. Recently, UV photolithography^[27,28] and multiphoton lithography^[29] have been successfully used to create 2D and 3D arbitrary microscale structures with naturally regenerated silk proteins (including both fibroin and sericin) as the resist. These resists are chemically modified to be photoreactive and also require arguably hazardous photoinitiators and developers, which significantly affect the flexibility of material choice and interfere with the biological functions. Furthermore, current protein-based bioresists still suffer from issues such as relatively low resolution and pattern contrast, mainly due to the inevitable large molecular weight distribution, which hinders their wide-range use in precise biopatterning. Proteins with well-defined molecular structures (such as the defined chain length, sequence, and

side chain groups for appropriate application-specific modification) are needed for versatile bionanopatterning.

Here, we report precise nanostructuring on genetically engineered spider silk by accurately directing ion and electron beam interactions with the protein's matrix at the nanoscale (which varies its solubility in water) to create a set of well-defined bionanoarchitectures for: (1) structure-enhanced fluorescence and (2) controlled cell seeding and inhibition as proof-of-concept demonstrations. The reduced scattering of ion beams in the resist material enables exceptional pattern precision and the added control over protein sequences and molecular weights of genetically engineered spider silk provides unprecedented lithographic resolution, sharpness, and biological functions compared to the natural proteins. Moreover, we report a creative strategy of building arbitrary grayscale (2.5D) and 3D bionanoarchitectures containing well-defined protein units serving as the building blocks with both shape and function on demand—termed “Protein Bricks.” Structures with high aspect ratio can be easily created while no hazardous chemicals (e.g., photoinitiators, organic solvents) are used or generated. The assembly is realized by a combination of ion beam lithography (IBL, which crosslinks proteins from top to bottom) and electron beam lithography (which crosslinks proteins from bottom to top) steps in a programmable sequence with precise alignment. This approach provides a facile method for patterning and immobilizing biomolecules within nanoscopic, hierarchical protein structures that could serve as the building blocks for functional nanocomponents and nanodevices.

The proposed process is schematically shown in Figure 1a. Recombinant spider silk proteins are designed and expressed

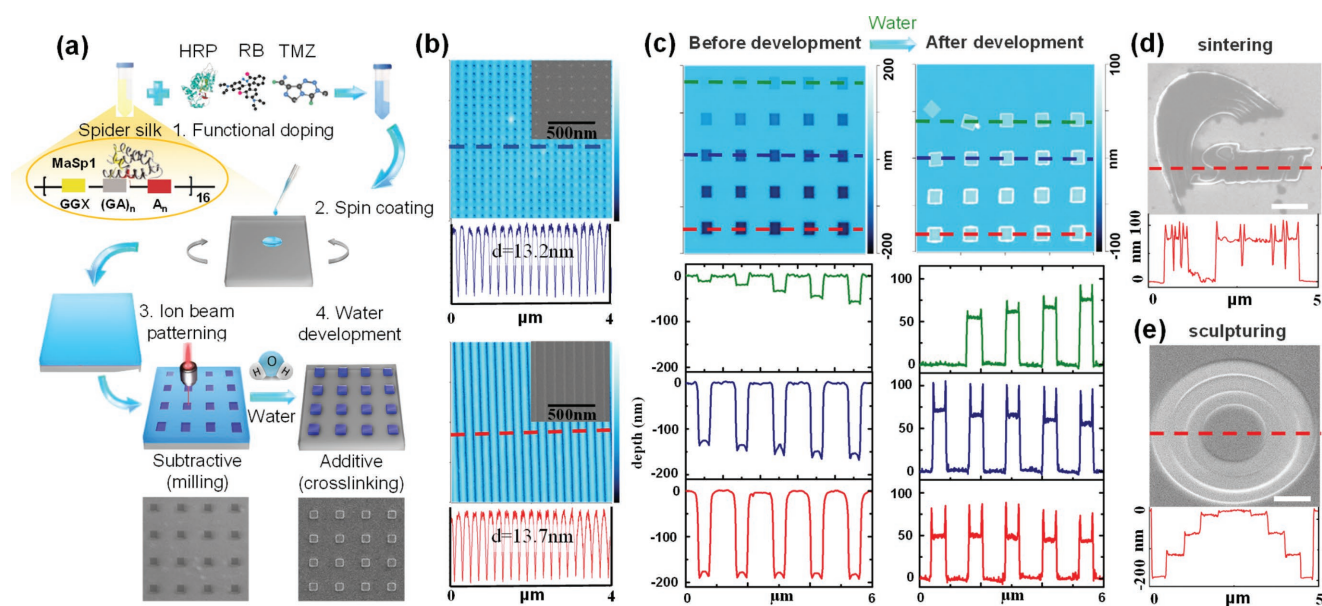


Figure 1. Precise nanopatterning on genetically engineered spider silk. a) The schematic process of bionanomanufacturing using IBL and genetically engineered spider silk proteins. The spider silk can be functionalized via simple mixing and spin-coated into thin films. The IBL writing can define two complementary types of nanostructures simultaneously, namely, nanosculpturing (subtractive by etching) and nanosintering (additive by crosslinking). The scanning electron microscopy (SEM) images of the nanoholes and nanopillars are shown below the schematics. b) Dot and line arrays fabricated using IBL on 30 nm thick spider silk film with a minimum feature size of 13.2 and 13.7 nm, respectively. c) The atomic force microscopy (AFM) images (left) of nanopatterns (before and after development in water) fabricated by nanosculpturing and nanosintering under different ion beam dosages ranging from 10 to 1500 $\mu\text{C cm}^{-2}$ (see Figure S3, Supporting Information for more details) and the topological profiles corresponding to the dotted line on the top. d, e) SEM images of 2D and grayscale patterns fabricated by IBL with the cross-section profiles on the bottom. The scale bar is 1 μm .

in *Escherichia coli* through genetic engineering (Please see Experimental Section for details). The purified aqueous recombinant spider silk solution can be functionalized with a variety of chemical and biological dopants such as fluorescent dyes, enzymes, and antibodies through a simple mixing process. The pure or functionalized spider silk solution is then spin-coated into thin films with thickness ranging from dozens of nanometers to several micrometers determined by the solution concentration and spinning speed. To define the nanoscale structures on the spider silk film, an IBL writing tool (strata FIB 201, FEI Co., USA) is used for nanometer-precision patterning.^[30] Dot and line arrays fabricated using IBL on 30 nm thick spider silk film with the minimum feature sizes of 13.2 and 13.7 nm respectively are successfully demonstrated (Figure 1b), approaching the molecular limits of the as-used recombinant spider silk proteins of ≈ 10 nm.^[25,26] The ion irradiation has two effects on the spider silk. First, high energy ions can etch off the spider silk, similar to what has been commonly observed in other materials.^[31] Meanwhile, the ions that penetrate into the film can induce structural transitions (crosslinking) in the spider silk from an amorphous state (soluble in water) to a more ordered β -sheet state (insoluble in water). The etching effect requires more energy than that for crosslinking and happens only at the surface of the film; while the crosslinked structures can form underneath the areas that are etched off by ions. Compared to nanopatterning of silk proteins using EBL in previous work,^[31] two complementary types of structures can be fabricated by a single step of IBL writing as shown in Figure 1c. The ion irradiation can etch the film according to the pre-designed nanoscale patterns in a subtractive fashion (referred to as “nanosculpturing” in this work) with increasing depth as the irradiation dosage increases from 10 to 1500 $\mu\text{C cm}^{-2}$. Simultaneously, the complementary nanoscale patterns are formed underneath the etched patterns and built additively with increasing height caused by more ion irradiation (referred to as “nanosintering” in this work). As a result of the way that the nanosintered patterns are formed, the structure can only survive the water development step and be left on the substrate when the ion irradiation dosage is above a threshold value (related to the thickness of the film). This is experimentally confirmed as shown in Figure 1c where the top row of a nanosintered pattern (with low irradiation dosages) is blank. As the ion irradiation dosage increases, the nanosintered patterns will be formed further down and closer to the bottom, at which point the patterns remain after water development, but move away from the designed location due to the lack of strong anchorage on the substrate. When the irradiation dosage is sufficiently high, the patterns stay on the substrate as expected, and edges will be formed when the dosage of the ion beam are large enough to crosslink the amorphous spider silk adjacent to the designed structures. However, the edges can be completely avoided at carefully controlled ion dosages.

To further exploit the characteristics of this fabrication paradigm, a 2D “SIMIT” logo and a grayscale (in terms of the height of the structure, or 2.5D) concentric ring nanostructure are fabricated by nanosculpturing and nanosintering respectively as presented in Figure 1d,e. As a more explicit manifestation of the quality and the grayscale nature of the nanostructures,

topologic profiles of both structures are shown together with their SEM images (more examples are shown in Figure S1, Supporting Information). The as-fabricated structures display a relatively smooth surface and vertical side walls. In addition, the minimum dosage to fabricate patterns on a 215 nm thick spider silk film at 30 keV is found to be 100 $\mu\text{C cm}^{-2}$ — $\approx 1/20$ of the dosage needed to fabricate comparable structures with EBL (25 keV), thus allowing high yield nanomanufacturing.^[13,14]

To explore the nanoscale conformational transitions of spider silk proteins, we prepare a set of spider silk samples on silicon substrates using IBL with nanoscale lithographic resolution. By exposing the spider silk film with dosages ranging from 10 to 840 $\mu\text{C cm}^{-2}$ (SEM images of the full range are shown in Figure S2, Supporting Information), three significantly different stages with different etching rates were observed before and after the water development (Figure 2a). With increasing dosages, the slope (plotted as etching depth against ion irradiation dosage, which is correlated with either the etching speed in the nanosculpturing or the structure formation speed in the nanosintering) of the three stages changes, indicating that the composition as well as the properties of the material are changing. The pattern depth of the undeveloped film shows the ion etching effect, whose speed is inversely proportional to the density of the material. Therefore, as the ion irradiation dosage increases, the density of the exposed spider silk also increases at three different stages, indicating the existence of conformational transitions. On the other hand, the height of patterns after development (red curve) also shows three stages as the ion irradiation dosage increases. For Stage I, the height of the patterned structures increases with ion dosage as the structure starts to form. However, Stages II and III show the opposite behaviors, where higher dosages result in lower structure height, which can be associated with the etching effect from higher ion irradiation dosage. The interaction between ions and spider silk with different film thickness was also investigated (see Figure S3, Supporting Information).

We postulate the molecular structures of the patterned spider silk as well as the etching/crystallization mechanism occurring in three different phases. Figure 2b is the schematic of the proposed spider silk fibroin conformational transitions induced by IBL with different ion irradiation dosages. The low dosages (Stage I) can crosslink the random coil to α -helix and β -sheet, making it water-insoluble. The subsequent “water development” results in dissolution of the amorphous silk, leaving the exposed area on the substrate, which forms nanoscale pillars. However, the beam dosage is not large enough to crosslink the patterns to the bottom, and thus, after water developing, the patterns can shift, rotate, and deviate from the original processing position. For medium ion beam dosages (Stage II), with an increase of ion beam dosage, the etching depth increases as well, allowing the designed patterns to reach the bottom of the spider silk film. The crystalline silk can be partially decrosslinked further to short polypeptides or even etched off with extra ion beam exposure. The spider silk protein can be burned (carbonized) at higher ion beam dosage (Stage III) and completely loses its structure, resembling previously reported work.^[32,14] This is attributed to the decomposition of peptide chains along with partial formations of carbonaceous pyroprotein after excessive

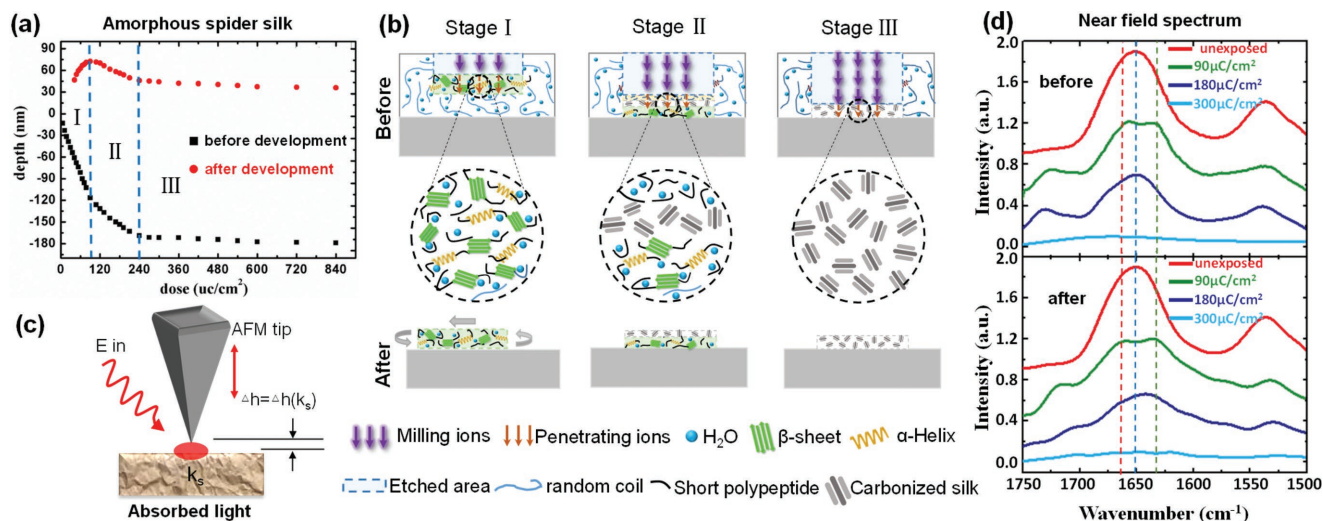


Figure 2. Nanoscale analysis of conformational transition of spider silk proteins under ion irradiation. a) The etching depth (black squares) and pattern height (red dots) of protein nanostructures with changing ion beam dosages show three distinct stages, indicating conformational and property changes at the three stages. b) The postulated mechanism of conformational transitions of the three different stages. For Stage I, the low ion beam dosage can crosslink the amorphous spider silk to the crystalline state, but the formed structure cannot reach the bottom of the film so to firmly anchor the substrate. Therefore, the patterns can shift, rotate, and deviate from the original patterning position after water developing. For Stage II, the ions can reach the bottom of the spider silk film, etch the crosslinked patterns, and break crosslinked structures to small peptide on the top surfaces of the fabricated patterns. For Stage III, when the dosage is large enough, the entire structure can be carbonized. c) Schematics of nanoscale IR spectroscopic measurement using AFM-IR. The thermal expansion due to absorption of IR light is used to map absorption characteristics of the spider silk. d) The IR near field spectra of patterns before and after development upon different ion beam irradiations of 90, 180, and 360 $\mu\text{C cm}^{-2}$. The characteristic peaks are 1631 cm^{-1} (β -sheet, green dash), 1650 cm^{-1} (random-coil, blue dash), and 1662 cm^{-1} (α -helix, red dash), respectively. The curves show that with low ion beam dosages, the amorphous spider silk is crosslinked into more ordered state (α -helix and β -sheet). As the dosage increases, the crosslinked spider silk is broken down into short peptides marked by the decrease in the characteristic absorption of β -sheet structure. Higher dosages of ion beam irradiation can carbonize the protein.

ion irradiance treatment of β -sheet nanostructures, as indicated by the Raman spectrum in Figure S4 (Supporting Information).

The mechanism of the structural transitions of spider silk proteins upon ion beam irradiation is studied by a comprehensive investigation of the ion beam-induced modification of silk at the nanoscale using a nondestructive near-field atomic force microscopy based infrared (AFM-IR) optical microscope (Anasys Instruments, USA). The simplified schematic of the nanoscale IR spectroscopy using AFM-IR is shown in Figure 2c. Localized thermal expansion due to the absorption of IR light is detected by a contact mode AFM tip, and the spectrum of the materials can be obtained by sweeping the wavelengths of the incident IR laser (Daylight Solutions, USA). The conformational transitions of the spider silk protein are investigated by analyzing the transition between amorphous and ion-beam-modified spider silk fibroin with an ion beam dosage of 90, 180, or 300 $\mu\text{C cm}^{-2}$, corresponding to the three stages, respectively (shown in Figure 2d). The spectrum of the amorphous spider silk (red line) shows an absorption peak centered at 1650 cm^{-1} , representing the typical random coil structures in the amorphous protein. The spectrum of the amorphous spider silk after being exposed to IBL of 90 $\mu\text{C cm}^{-2}$ (Stage I, green line) shows two peaks at 1662 and 1631 cm^{-1} , typical of the α -helix and β -sheet conformation of spider silk proteins, respectively.^[33] Compared to the amorphous spider silk before ion irradiations, the proportion of random-coil is decreased, and the α -helix and β -sheet content is increased, indicating the random-coil

component can be crosslinked to crystalline structures through the irradiation of ion beam. For 180 $\mu\text{C cm}^{-2}$ (Stage II, purple line), the proportion of random coils increases again, which means the crystalline structures can be decrosslinked with extra ions interaction. For 360 $\mu\text{C cm}^{-2}$ (Stage III, blue line), the characteristic peaks of spider silk proteins gradually vanish, indicating that most of the protein structures are carbonized with large dosage. Meanwhile, we collected near-field images at 1631 cm^{-1} (the typical β -sheet absorption peak) for the three stages. The comparison of signal intensities in near-field images for Stage II at different wavenumbers is shown in Figure S5 (Supporting Information). In addition, the conformational transitions of the crystalline spider silk under ion irradiations were investigated in a similar fashion (please see Figure S6, Supporting Information).

Compared with electrons, ions are much heavier, and can maintain better propagating direction due to the smaller scattering rate inside the materials. The ion scattering in three resist materials—namely polymethyl methacrylate (PMMA), naturally extracted silk fibroin, and genetically engineered spider silk—are simulated by The Stopping and Range of Ions in Matter (SRIM, SRIM Co. USA) software (Figure 3a). Trajectories of the Ga^+ ions in the three materials are obtained by setting the ion source (Ga^+), ion voltage (30 kV), film thickness (100 nm), film density (1.2 g cm^{-3} for spider silk, 1.3 g cm^{-3} for silk fibroins), and incident ion number (50) as the simulation parameter. The statistics of penetration depth as well as alignment (defined as depth/straggle) are then calculated from the simulation. The simulation

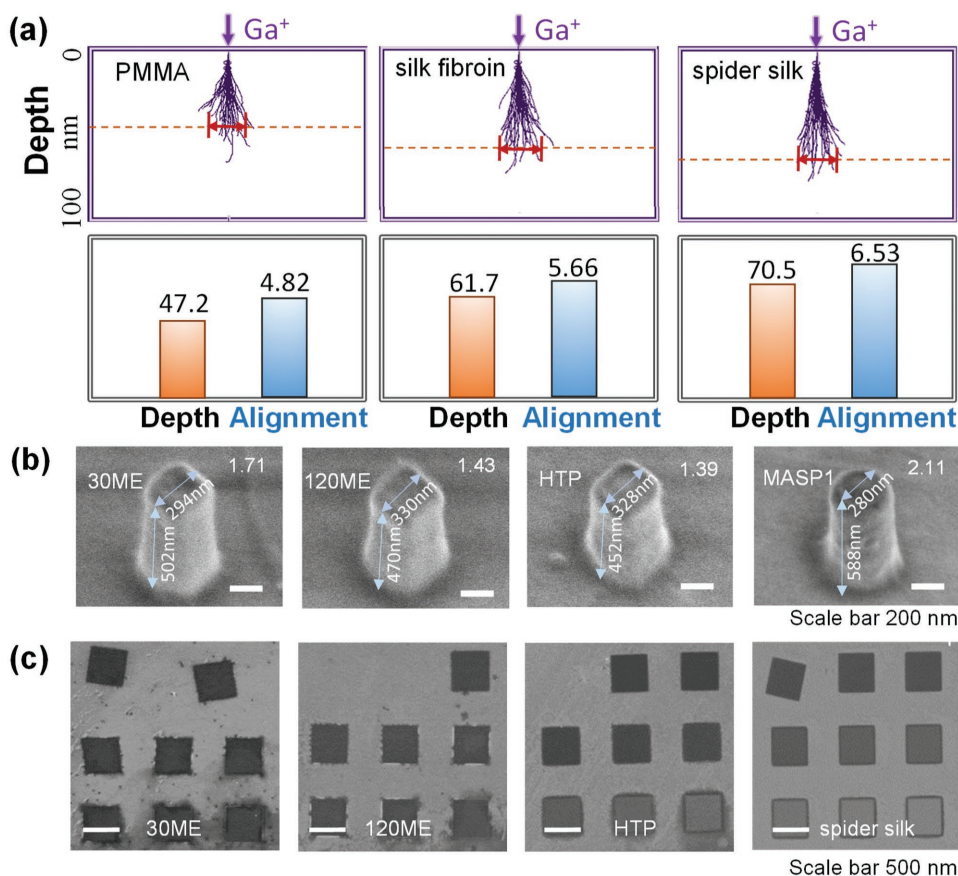


Figure 3. Performance evaluation of nanopatterning on natural and synthetic silk proteins. a) The ion distribution in different polymeric materials (PMMA, natural silk fibroin, and recombinant spider silk). The top row shows the simulated trajectories of ions in different materials. The dashed line represents the penetration depth of ions. And the bottom row is the calculated depth and alignment of ion propagation in different materials. The alignment is defined as depth/straggle. b) The comparison between different materials in terms of experimentally achieved maximum structure aspect ratio. c) SEM images of naturally extracted silk fibroin proteins and genetically engineered spider silk protein fabricated using IBL with change of dosage (increasing from the top left corner of $30 \mu\text{C cm}^{-2}$ to the bottom right one of $1500 \mu\text{C cm}^{-2}$) to compare the fabrication sensitivity and contrast. Some patterns on the top row are drifted because the ion irradiation dosages are not high enough to crosslink the fibroin protein down to the bottom. Therefore, those patterns are not anchored well on the substrate.

and the statistics show that the genetically engineered spider silk (with a penetration depth of 70.5 nm and alignment of 6.53 nm/nm) has a longer penetration depth and better alignment than both the silk fibroin (with a penetration depth of 61.7 nm and alignment of 5.66 nm/nm) and the PMMA (with a penetration depth of 47.2 nm and alignment of 4.82 nm/nm). This is mainly determined by the fact that when the ions penetrate into the silk films, the films with smaller molecular chains can make less resistant to the incident ions, permitting larger ion penetration depth. Meanwhile, the penetration depth of H^+ , He^+ , and other ions in spider silk are simulated using SRIM (please see Figure S7, Supporting Information). Since H^+ and He^+ are much smaller, the penetration depth can be as large as 2.5 and 1.8 μm at 200 kV acceleration voltage.

Another important benchmark in the performance evaluation of nanopatterning is the maximum achievable aspect ratio of the fabricated nanostructures—one of the main factors that limit the complexity of the nanostructures. We study the aspect ratios of the fabricated nanostructures using silk fibroin protein extracted for 30 min (30 ME silk) and 120 min (120 ME silk),

silk fibroin extracted under 121 °C temperature and 1.2 kPa pressure (HTP silk), and recombinant Major Ampullate Spideroins 1 (MaSp1)^[25] as shown in Figure 3b. Benefitted from the high alignment, the structures fabricated using IBL generally have good aspect ratios. The 30 ME silk fibroin displays an aspect ratio of 1.71, which is better than the 120 ME (1.43) and HTP (1.39) silk. This is due to the fact the 30 ME silk has the longest average protein chain lengths and therefore, better mechanical properties to sustain structures with high aspect ratios. On the other hand, the MaSp1 spider silk exhibits structures with a superior aspect ratio (2.11) to the 30 ME silk, indicating even better mechanical strengths. Note that there is a trade-off between the mechanical strength and ion penetration depth in natural silk. But for the genetically engineered spider silk (such as MaSp1), the mechanical strength can be optimized by redesigning the amino acid sequences of the proteins, such as increasing the proportion of (GA)_n and An modules, which is responsible for high strength of spider silk. In that case, so that both large mechanical strength and penetrate depth could be achieved.

In addition, a series of nanostructures with increasing dosages from 30 to 1500 $\mu\text{C cm}^{-2}$ are fabricated according to the nanosintering process using the same set of materials (i.e., 30 ME silk, 120 ME silk, HTP silk, and MaSp1 spider silk) to evaluate their IBL sensitivity and sharpness (Figure 3c). The smallest dosage at which the fabricated structure can stay on the substrate is correlated with the sensitivity of the material while the pattern sharpness indicates the contrast. The patterns fabricated using recombinant spider silk show the best completeness, which suggests that the structures can reach the bottom of the substrate with smaller ion irradiation dosages compared with the silk fibroin-based material and thus have higher IBL sensitivity. These properties can be mainly attributed to the lower density and shorter chain length of the spider silk since the ions can penetrate and crosslink the film easier. In addition, because of the well-defined and uniformly distributed molecular weight, the spider silk exhibits the best pattern sharpness as shown in Figure 3c. For a comprehensive study of the material behavior, comparisons of other properties (such as the etching selectivity and glass transition temperature) between the spider silk and other polymeric materials are also investigated, and the results are shown in Figure S8 (Supporting Information).

One of the main advantages of using spider silk is its ease of functionalization through simple mixing with organic and inorganic dopants in the water-based solution, bringing function to programmable nanoscale forms. In addition to being used as the hosting matrix, the spider silk can preserve the activities of the dopants such as enzymes and antibodies. As a proof-of-principle demonstration of the genetically engineered spider silk doped with biologically functional molecules, horseradish peroxidase (HRP) is mixed into the spider silk matrix (Figure 4a). The doped spider silk is then spin-coated on silica substrates for better color observation. Two sets of samples are prepared where half of each substrate is washed to remove the spider silk for use as control groups (marked “ctr”). The sample areas with spider silk left (marked “sam”) are then patterned with a simple square matrix using nanosintering and nanosculpturing techniques, respectively. With the addition of 3,3',5,5'-tetramethylbenzidine (TMB) droplets, a color change (from colorless to blue) can be observed if the TMB reacts with active HRP. The HRP-doped spider silk samples can well maintain the activity of the dopant even after Ga^+ ion irradiation (Figure 4a).

The doped spider silk can also be fabricated into structures that achieve shape-enabled functions. As a demonstration of this concept, the genetically engineered spider silk is doped with fluorescent dye that emits light at a center wavelength of 580 nm (Figure 4b). The doped spider silk is then fabricated into optical nanogratings. With an additional thin layer of silver (Ag) deposited on top, the fluorescent light can be enhanced due to surface plasmon effects. Spectra of samples prepared with different grating periods ranging from 500 to 650 nm are collected using a micro-photoluminescence spectroscopy (Carl Zeiss A1, Germany) with an excitation wavelength of $\lambda = 532$ nm. As shown in Figure 4b, the fluorescent intensity can be clearly enhanced (≈ 9 fold) with the grating structure, where the best enhancement is achieved with a grating periodicity of 580 nm, matching the emission spectrum of the fluorescent dye. This proves the applicability of the structure assisted functional spider silk as a platform for enhancing the functions of its dopants.

Furthermore, the biocompatibility of the patterned spider silk enables cellular level functions such as guided cell seeding and inhibition by doping with bioactive materials. Two examples are demonstrated in Figure 4c. A mesh structure is fabricated using the nanosintering protocol on a spider silk film mixed with collagen, which promotes cell adhesion,^[34] and neuronal cells/glioma cells are then cultured on the substrate by following the protocol described in the Experimental Section.^[35] As illustrated in Figure 4c, the neuronal cells adhere closely according to the fabricated patterns. The cells that proliferate along the patterned area are counted against the pattern-void area respectively (with a ratio of 169:16), quantitatively justifying that the fabrication paradigm can be used for devices that achieve cellular level functions. Alternatively, a similar mesh structure is patterned using spider silk doped with temozolomide (TMZ), which is an alkylating agent used as a treatment of brain cancers. The activity of the TMZ in the fabricated mesh structures is verified by culturing cancer cells on the substrate. The fluorescence image in Figure 4c shows that few cancer cells can live on the pattern area, and therefore proves the inhibition function of the TMZ doped in the spider silk matrix. A ratio of 7:201 is also obtained by counting the cancer cells on and away from the patterned area to quantitatively show the effectiveness of the doped TMZ. Notably, unpatterned genetically engineered spider silk was also proved to be biocompatible by neuron and glioma cells culture (Figure S9, Supporting Information).

To take advantage of the fabrication and doping flexibility, we use a combination of IBL (crosslink from top to bottom) and EBL (crosslink from bottom to top)—termed as “IEBL” thereafter—to manufacture a variety of complex 3D functional nanostructures which are difficult to make otherwise. Borrowing the concept from a popular type of toy (where large architectures can be constructed using basic blocks with different geometries), we designed a set of basic blocks with increasing geometric complexity, which can be “assembled” to make composite shapes. Simple geometries (first row), planar combinations of simple geometries (second row), geometries with both nanosintered and nanosculptured structures (third row), and geometries with two nanosintering and nanosculpturing levels are sketched (Figure 5a) and fabricated (Figure 5b) by IEBL. Figure 5c is the schematic of a two-step lithography process of IEBL used to precisely fabricate a miniaturized spider silk nanodesk consisting of nanoscale Protein Bricks. A layer of amorphous spider silk (containing mostly random coils structures) film with a thickness of 1.1 μm is spin-coated on silicon substrate, followed by an EBL writing step that constructs a series of nanopillars (diameter: 300 nm) from the bottom to the top of the film, providing stable support for subsequent processing. Next, a second step of IBL was used to induce localized structural transitions in only the top part of the spider silk film by precisely controlling ion irradiation dosage. By precisely controlling ion irradiation dosage, the molecular chains of the overlapped area can interact with each other through chain entanglement and hydrogen bonding, which is analogous to the assembly of two toy building blocks. At last, water development was performed to reveal the 3D nanostructures.

A couple of examples have been realized by following the procedure described above. Protein nanodesks are produced by

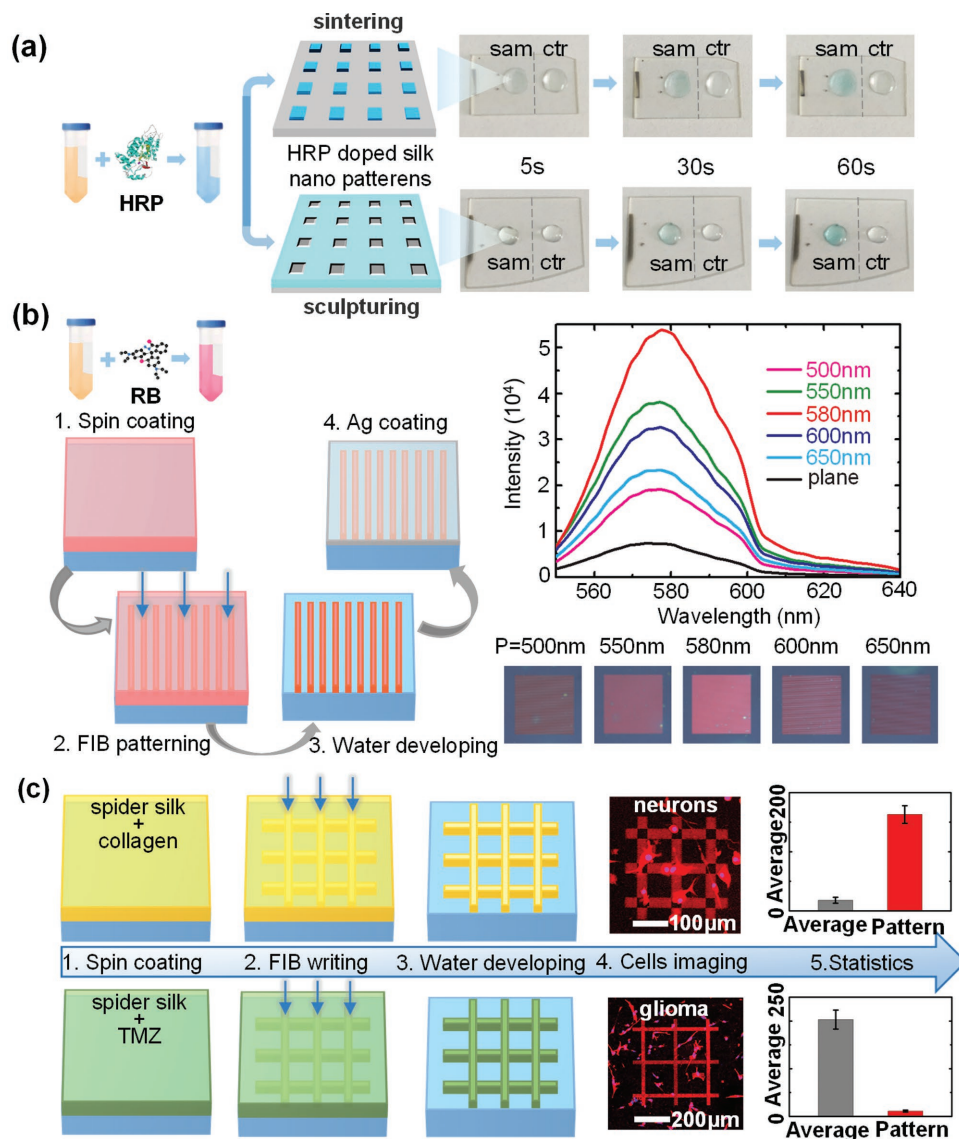


Figure 4. Functionalization of silk nanostructures via facile doping with functional molecules. a) Enzyme activity assessment of horseradish peroxidase doped in the spider silk after both nanosintered (the top row) and nanosculptured (the bottom row) nanopatterning processes. The HRP-doped spider silk is spin-coated on silica substrates for IBL nanofabrication. The left part (“sam”) is the patterned spider silk, and the right part (“ctr”) is the control group on bare silica substrates for comparison. By adding tetramethylbenzidine solution on both sides, a chromogenic reaction is observed on the left, indicating preservation of bioactivity of the enzyme in spider silk matrix after ion irradiation. b) The spider silk protein doped with fluorescent molecules (e.g., RB) is fabricated into optical grating structures. The deposited layer of Ag onto the optical gratings can enhance the fluorescence significantly due to surface plasmon effects. The fluorescent spectra and microscope images of plane surface and nanostructures with different periodicities are shown on the right. c) The schematic of spider silk patterns doped with collagen/TMZ doped for appropriate functionalization. The functionalized protein structures can guide the proliferation of neural cells or inhibit the growth of cancer cells. The cells imaging and statistics are presented on the right to show the quantitative data. The gray graph represents the number of cells in the unpatterned area, and the red graph represents the number of cells that proliferate along the patterned area.

forming the legs with EBL and desktop with IBL (Figure 5d). The desktop (with an area of $3 \mu\text{m} \times 3 \mu\text{m}$ and a thickness of only 50 nm) is able to maintain its shape with only one additional support at the center in addition to the four desk legs (diameter: 300 nm) at the corner. Furthermore, nanoscale spider webs (with a diameter of $3 \mu\text{m}$ and a strand thickness of 50 nm) are also demonstrated in Figure 5e by fabricating the supporting pillars with EBL and the spider web lines with IBL (Detailed assembly steps are show in Figure S10, Supporting

Information). The fluorescent images of fluorescein sodium (green)-doped and Rhodamine B (RB, red)-doped spider silk nanoweb demonstrate the 3D nature of the nanoweb where the RB-doped nanoweb is folded due to the intentional removal of two of the anchor points of the nanoweb, whose 3D nature is otherwise difficult to reveal using our current confocal imaging set up due to the small geometries, especially in the z-direction. Similar results have been successfully achieved with genetically engineered fluorescent spider silk (Figure S11, Supporting

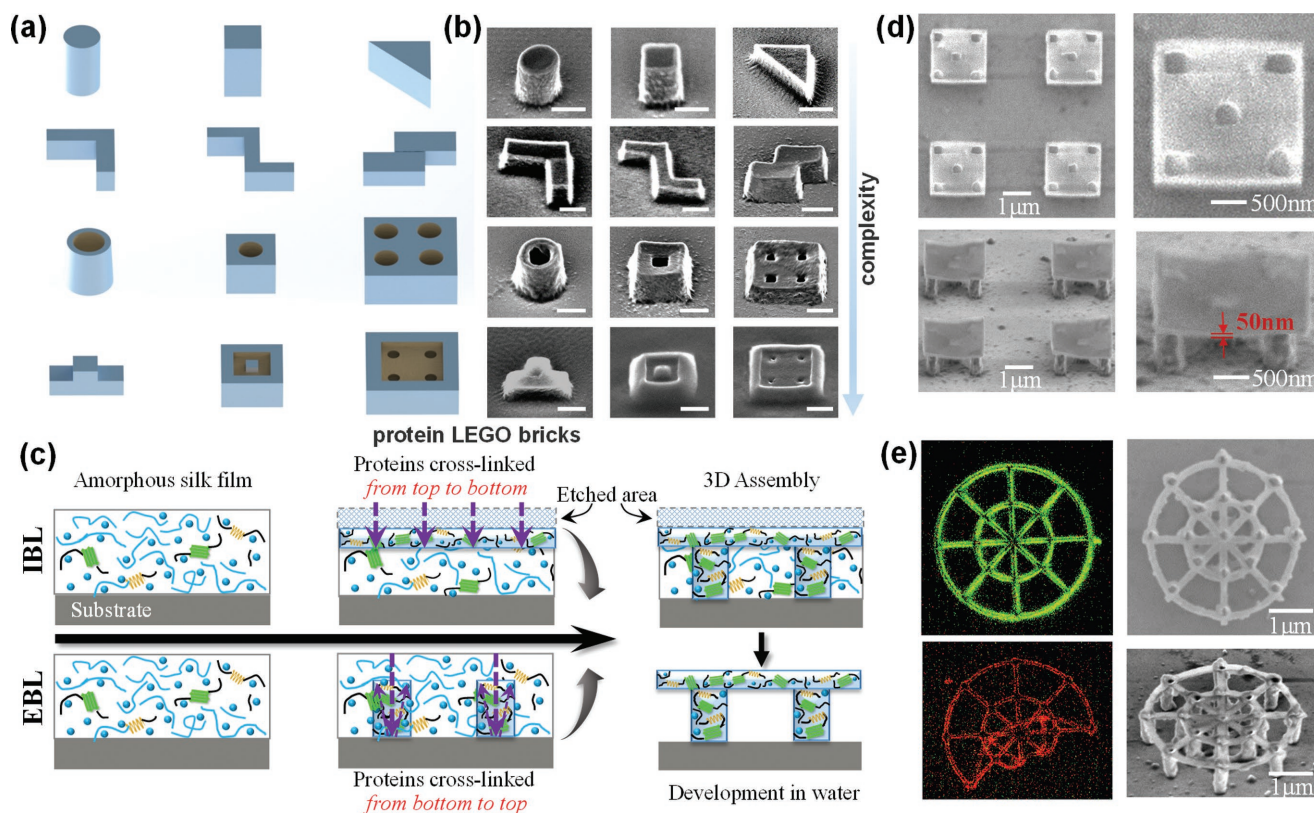


Figure 5. Manufacturing and assembly of 3D bionanoarchitectures via Protein Bricks using IEBL. a) The sketches of the designs, and b) the SEM images of the fabricated nano Protein Bricks blocks with increasing geometry complexity. The scale bar is 500 nm. c) Creating 3D nanostructures with IEBL. d) The SEM images of 3D nanodesks via Protein Bricks. e) The fluorescent (left) and SEM (right) images of 3D spider nanowebs via IEBL on fluorescein sodium (green)-doped and RB (red)-doped spider silk. Note that, for the RB-doped spider web, two of the anchoring points were intentionally neglected such that the unsupported part can fold during the water development, showing the 3D nature of the fabricated structure.

Information). The fact that both the thin desktop and the delicate spider web lines can survive the water development step and sustain their designed shapes is a manifestation of the exceptional mechanical strength of the genetically engineered spider silk and the reliability of this fabrication paradigm. In addition, heterogeneous, hierarchical silk structures in the form of biomimetic spider webs can be realized either laterally or vertically using different types of genetically engineered spider dragline silk proteins MaSp1 and MaSp2 known for their outstanding mechanical strength and elasticity respectively, which are further modified with different functions (e.g., red and green fluorescent, respectively), underlining the flexibility and versatility of this platform.

The unique combination of genetically engineered spider silk and IEBL fabrication technique, Protein Bricks, offers extensive versatility for a variety of applications that require devices to be produced in a “green” way with customizable biofunctions and accurate nanoscopic geometries, and serves as a promising route to complement current 3D bionanofabrication techniques such as DNA origami and multiphoton lithography, thanks to its capability of fabricating multiscale structure with facile functionalization. DNA origami offers advantages of fine structural resolution and complexity with typical structure dimensions in the 1–100 nm range by designing the sequence of staple strands and controlling the subsequent self-assembly

process with careful management of temperature, pH value, and time.^[36] However, self-assembly with longer DNA strands has suffered from extremely low yields even for simple geometries due to the complexity of folding a very large DNA strand into a compact shape. On the other hand, multiphoton based 3D lithography has been demonstrated to fabricate arbitrary micron-sized 3D structures with ease.^[37] By employing oil immersion and two-photon dyes, sub-micron structures were also successfully demonstrated. However, it still suffers from low resolutions (especially in the z-direction) and involves the usage of toxic substances that compromise the biological activity and restrict the functionalization of biomaterials. The “length scale gap” between 3D biostructures that can be readily fabricated by DNA origami via molecular assembly (relatively comfort zone: 1–100 nm)^[38] and multiphoton lithography using biomaterials (relatively comfort zone: >500 nm) can be fulfilled by the reported Protein Bricks method with reduced process complexity and enhanced flexibility of functionalization (Figure S12, Supporting Information).

To extend the capability of our methods, more complex and multifunctional structures can be realized by stacking multiple layers of spider silk protein together, where each layer can be individually fabricated with the desired geometries. What is more appealing is that for each layer, the genetically engineered spider silk can be “customized” to specific duties for part of a

larger task. For instance, the spider silk itself can be modified through genetic engineering to have innate tunable properties such as elasticity, hydrophobicity, and molecular weight, as well as through side group conjugation using chemical methods (e.g., UV-sensitization).^[27] In addition, by simple doping the spider silk solution with various types of inorganic and organic molecules, the recombinant spider silk can acquire many different functions. It can also be mixed together with other proteins to serve as hybrid materials (e.g., largely tunable mechanical properties and cell adhesion by mixing with collagen at different ratios). This multiplex of functionality in addition to on-demand nanoscale composite structures adds an entire new dimension to the versatility of this platform. The structural complexity and ease of functionalization achieved by Protein Bricks is essential in applications, such as microenvironment reconstruction, cell sorting, and biomimetic devices.

Concerns may arise regarding the possible ion contamination during IBL process because the Ga⁺ ions could disturb the biocompatibility of the fabricated device, rendering it unsuitable for bioapplications. To meet this challenge, we demonstrate successful guided cell seeding and inhibition using prepatterned functional spider silk substrate in this work, which suggests that the ions do not have a significant effect on the cytocompatibility of the fabricated device. This can be further improved by utilizing IBL system based on inert Helium (He) ion, which offers better fabrication resolution thanks to the lower divergence of He ions in the vicinity of sample surface.^[39]

In summary, we report creating 2D and 3D bio-nanostructures with shape and function on demand using a two-step IEBL process on genetically engineered spider silk proteins via a newly reported strategy of Protein Bricks, which provides a versatile platform to perform multifunctional 3D nanostructuring for current and emerging biomedical applications.

Experimental Section

Silk Solution Preparation: Silkworm silk fibroin proteins were prepared using established purification protocols. *Bombyx mori* cocoons were boiled for 30 min in aqueous 0.02 M Na₂CO₃ (Sigma-Aldrich, USA) and then rinsed for 3 × 30 min in distilled water to remove the Na₂CO₃ and sericin. The degummed cocoons were allowed to dry for more than 12 h and then subsequently dissolved in 9.3 M LiBr (Sigma-Aldrich, USA) solution at 60 °C for 4 h. The solution was dialyzed for 2 d in distilled water using Slide-A-Lyzer dialysis cassettes (Molecular weight cut-off, MWCO 3500, Pierce, USA). The solution was centrifuged for 2 × 20 min at 18 000 rpm. The concentration was determined by measuring a volume of solution and the final dried weight.

Recombinant Spider Silk Preparation: Recombinant plasmids were constructed that encoded a dragline silk-like protein MaSp1 having 16 repetitive units flanked by the N- and C-terminal domains of the spider *Nephila clavipes*. The recombinant silk proteins were prepared according to the previously reported protocols.^[25] Briefly, *E. coli* BL21 (DE3) cells harboring the silk expression plasmid were treated with isopropyl-β-D-thiogalactopyranoside at 1 × 10⁻³ M for ≈ 6 h to induce silk expression. The induced cells were then harvested and resuspended in a binding buffer (10 × 10⁻³ M Tris-HCl, 150 × 10⁻³ M sodium chloride, 5 × 10⁻³ M imidazole, pH 8.0). After sonication to disrupt the cells, the mixture was centrifuged at 9 000 g for 20 min at 20 °C and the supernatant was loaded onto a column with precharged Ni sepharose which had been equilibrated with the binding buffer. The column was washed with buffer (10 × 10⁻³ M Tris-HCl, 150 × 10⁻³ M

sodium chloride, 60 × 10⁻³ M imidazole, pH 8.0) and eluted with buffer (10 × 10⁻³ M Tris-HCl, 50 × 10⁻³ M sodium chloride, 150 × 10⁻³ M imidazole, pH 8.0). The eluent was dialyzed for 2 d against distilled water using Slide-a-Lyzer dialysis cassettes (MWCO 3500, Pierce, USA). The purity of protein samples was determined by sodium dodecyl sulfate polyacrylamide gel electrophoresis.

Nanoscale Infrared Spectroscopy and Imaging Using s-SNOM: A commercial scattering scanning near-field optical microscope (s-SNOM, Anasys Instruments Co, USA) with a QCL IR laser (Daylight Solutions Inc., USA) that was tunable between 1490 and 1690 cm⁻¹ was utilized. The AFM was operated in tapping mode. Pt-coated AFM probes with 200–500 kHz resonance frequency were used to enhance the IR signal. The near field signal was detected simultaneously with AFM signals. The IR signal used for analysis in this work was measured by a lock-in amplifier at the second harmonics of the tapping frequency, which provided both reflection and absorption that were (mostly) free of background.

Infrared Nanospectroscopic Study Using AFM-IR: The IR spectrum was acquired using an AFM-IR system (Anasys Instruments, CA, USA). It allowed high spatial resolution (30 nm) and spectral resolution (1 cm⁻¹) IR absorption measurement using a combination of AFM and IR laser source. The AFM measured the local thermal expansion of the sample due to the absorption of the IR laser, and thereby mapped material absorption as a function of wavenumber. Topography images were scanned before the IR spectra measurement to precisely locate the point of interest. The spectrum was acquired in the range between 1490 and 1690 cm⁻¹, using multiregion laser power settings to ensure consistent signal to noise ratio. The spectrum data were averaged by 10 repeated scans on the same spot. Also, it was averaged by taking five measurements on adjacent spots (each with 10 scan averaging) with the same composition. The sample data were normalized with respect to the spectrum of silicon under the same ambient environment.

Fluorescence Spectra Measurement: The sample was excited from the top surface using micro-photoluminescence spectroscopy as an excitation source. The incident light was focused by an optical microscope objective with magnification of 100× onto the sample, and the emission was collected by the same objective.

Cell Culture: Embryonic neural stem cells and U251 glioma cells were acquired by the courtesy from Prof. Hongying Sha (State Key Laboratory of Medical Neurobiology, Fudan University, China). Embryonic neural stem cells were cultured in DMEM/F12 proliferative medium with additives of 20 ng mL⁻¹ bFGF, 10 ng mL⁻¹ EGF, 2% B27 in 25 cm² culture flask. After 2 d of culturing, cell number was adjusted to 1 × 10⁵ mL⁻¹. Spider silk Protein Bricks was placed into 6-well cell-culture plate (Corning) after sterilization. A pipette was used to transfer 5 × 10⁴ cells into each well supplemented with 2% fetal serum which made it adhesive to spider silk Protein Bricks, and the culture plate was placed in an incubator at a temperature of 37 °C, and regulated with 5% CO₂ for another 2 d. U251 was cultured in the medium of DMEM + 10% fetal serum, and transferred to 6-well cell-culture plate containing spider silk Protein Bricks similar to embryonic neural stem cells. Further experiment was proceeded after the cells were cultured.

Immunofluorescence: Immunofluorescence staining was performed as described previously. Primary antibodies were diluted as follows: human anti-Nesting 1:400 (Abcam, United Kingdom), human anti-GFAP 1:500 (Abcam, United Kingdom). Secondary fluorochrome-conjugated antibodies were diluted 1:1000 (mouse anti-human, Abcam, United Kingdom). Spider silk Protein Bricks loading with embryonic neural stem cells and U251 glioma cells were mounted with slides after treating with 0.25 μg μL⁻¹ DAPI (Sigma, USA) for counter-nuclear staining.

Cell Imaging and Statistical Analysis: Cell imaging was performed by fluorescent microscopy (Carl Zeiss A1, Germany) with a magnification of 40×. Nine visual fields were captured according to each corresponding pattern. Cells grow on the pattern and outside the pattern were counted, respectively. Means were compared between two groups by Mann-Whitney U-test or Student's *t*-test, where appropriate. Statistical significance was defined as a *p* value < 0.05. Analyses were conducted using SPSS statistical software (version 23.0, IBM, USA).

Supporting Information

Supporting Information is available from the Wiley Online Library or from the author.

Acknowledgements

J.J. and S.Z. contributed equally to this work. T.H.T., X.X., and J.J. conceived and designed the experiments. J.J., S.Z., Z.S., N.Q., and L.S. performed the experiments. X.X., Z.Q., W.S., and L.S. contributed materials. J.J., T.H.T., S.Z., X.X., Z.S., S.N. G.C., X.C., M.L., D.L.K., and F.G.O. analyzed the data. T.H.T., J.J., and S.Z. wrote the paper. All authors discussed the results and commented on the manuscript. The work was partially supported by the MOST of China (Grant Nos. 2016YFA0200800 and 2016YFE0204400), the National Science Foundation under the CMMI Division (Grant Nos. 1563422 and 1562915), the National Natural Science Foundation of China (Grant Nos. 61574156, 61527818, 31470216, and 21674061), the Science and Technology Commission of Shanghai Municipality for the support under the International Collaboration Project (Grant No. 14520720400), 973 Program (Grant No. 2015CB755500), Natural Science Foundation and Major Basic Research Program of Shanghai (Grant No. 16JC1420100), Shanghai Natural Science Fund (Grant No. 16ZR1442500), National Natural Science Foundation of China (Grant Nos. 51703238 and 51703239), and Shanghai Sailing Program (Grant No. 17YF1422800).

Conflict of Interest

The authors declare no conflict of interest.

Keywords

biomaterials, bio-nanostructures, protein Bricks, spider silk

Received: October 11, 2017
Revised: January 23, 2018
Published online:

- [1] X. Liu, S. Wang, *Chem. Soc. Rev.* **2014**, *43*, 2385.
- [2] A. Kabashin, P. Evans, S. Pastkovsky, W. Hendren, G. Wurtz, R. Atkinson, R. Pollard, V. Podolskiy, A. Zayats, *Nat. Mater.* **2009**, *8*, 867.
- [3] M. Lutolf, J. Hubbell, *Nat. Biotechnol.* **2005**, *23*, 47.
- [4] J. B. Matson, S. I. Stupp, *Chem. Commun.* **2012**, *48*, 26.
- [5] D. Han, S. Pal, J. Nangreave, Z. Deng, Y. Liu, H. Yan, *Science* **2011**, *332*, 342.
- [6] X. Qu, D. Zhu, G. Yao, S. Su, J. Chao, H. Liu, X. Zuo, L. Wang, J. Shi, L. Wang, *Angew. Chem.* **2017**, *56*, 1855.
- [7] N. V. Voigt, T. Tørring, A. Rotaru, M. F. Jacobsen, J. B. Ravnsbæk, R. Subramani, W. Mamdouh, J. Kjems, A. Mokhir, F. Besenbacher, *Nat. Nanotechnol.* **2010**, *5*, 200.
- [8] J. Wang, J. Chao, H. Liu, S. Su, L. Wang, W. Huang, I. Willner, C. Fan, *Angew. Chem.* **2017**, *56*, 2171.
- [9] H. Zhang, J. Chao, D. Pan, H. Liu, Y. Qiang, K. Liu, C. Cui, J. Chen, Q. Huang, J. Hu, *Nat. Commun.* **2017**, *8*, 14738.
- [10] P. Tseng, B. Napier, S. Zhao, A. N. Mitropoulos, M. B. Applegate, B. Marelli, D. L. Kaplan, F. G. Omenetto, *Nat. Nanotechnol.* **2017**, *12*, 474.
- [11] G. M. Whitesides, B. Grzybowski, *Science* **2002**, *295*, 2418.
- [12] E. Bat, J. Lee, U. Y. Lau, H. D. Maynard, *Nat. Commun.* **2015**, *6*, 6654.
- [13] S. Kim, B. Marelli, M. A. Brenckle, A. N. Mitropoulos, E.-S. Gil, K. Tsioris, H. Tao, D. L. Kaplan, F. G. Omenetto, *Nat. Nanotechnol.* **2014**, *9*, 306.
- [14] Q. Nan, S. Zhang, J. Jiang, S. Gilbert Corder, Z. Qian, Z. Zhou, W. Lee, K. Liu, X. Wang, X. Li, *Nat. Commun.* **2016**, *7*, 13079.
- [15] J. J. Amsden, D. Peter, G. Ashwin, R. D. White, N. L. Dal, D. L. Kaplan, F. G. Omenetto, *Adv. Mater.* **2010**, *22*, 1746.
- [16] M. A. Brenckle, H. Tao, S. Kim, M. Paquette, D. L. Kaplan, F. G. Omenetto, *Adv. Mater.* **2013**, *25*, 2378.
- [17] D. Lin, H. Tao, J. Trevino, J. P. Mondia, D. L. Kaplan, F. G. Omenetto, L. D. Negro, *Adv. Mater.* **2012**, *24*, 6088.
- [18] H. Perry, A. Gopinath, D. L. Kaplan, L. Dal Negro, F. G. Omenetto, *Adv. Mater.* **2010**, *20*, 3070.
- [19] K. Salaita, Y. Wang, C. A. Mirkin, *Nat. Nanotechnol.* **2007**, *2*, 145.
- [20] M. B. Applegate, J. Coburn, B. P. Partlow, J. E. Moreau, J. P. Mondia, B. Marelli, D. L. Kaplan, F. G. Omenetto, *Proc. Natl. Acad. Sci. USA* **2015**, *112*, 12052.
- [21] D.-H. Kim, J. Viventi, J. J. Amsden, J. Xiao, L. Vigeland, Y.-S. Kim, J. A. Blanco, B. Panilaitis, E. S. Frechette, D. Contreras, *Nat. Mater.* **2010**, *9*, 511.
- [22] F. G. Omenetto, D. L. Kaplan, *Science* **2010**, *329*, 528.
- [23] G. Perotto, M. Cittadini, T. Hu, S. Kim, M. Yang, D. L. Kaplan, A. Martucci, F. G. Omenetto, *Adv. Mater.* **2015**, *27*, 6728.
- [24] H. Tao, D. L. Kaplan, F. G. Omenetto, *Adv. Mater.* **2012**, *24*, 2824.
- [25] X.-X. Xia, Z.-G. Qian, C. S. Ki, Y. H. Park, D. L. Kaplan, S. Y. Lee, *Proc. Natl. Acad. Sci. USA* **2010**, *107*, 14059.
- [26] X. X. Xia, Q. Xu, X. Hu, G. Qin, D. L. Kaplan, *Biomacromolecules* **2011**, *12*, 3844.
- [27] N. E. Kurland, T. Dey, C. Wang, S. C. Kundu, V. K. Yadavalli, *Adv. Mater.* **2014**, *26*, 4431.
- [28] R. K. Pal, A. A. Farhaly, M. M. Collinson, S. C. Kundu, V. K. Yadavalli, *Adv. Mater.* **2016**, *28*, 1406.
- [29] Y. L. Sun, Q. Li, S. M. Sun, J. C. Huang, B. Y. Zheng, Q. D. Chen, Z. Z. Shao, H. B. Sun, *Nat. Commun.* **2015**, *6*, 8612.
- [30] K. Keskinbora, C. Grévent, M. Hirscher, M. Weigand, G. Schütz, *Adv. Funct. Mater.* **2015**, *3*, 792.
- [31] Y. Greenzweig, Y. Drezner, S. Tan, R. H. Livengood, A. Raveh, *Microelectron. Eng.* **2016**, *155*, 19.
- [32] S. Y. Cho, Y. S. Yun, S. Lee, D. Jang, K. Y. Park, J. K. Kim, B. H. Kim, K. Kang, D. L. Kaplan, H. J. Jin, *Nat. Commun.* **2015**, *6*, 7145.
- [33] H. Yang, S. Yang, J. Kong, A. Dong, S. Yu, *Nat. Protoc.* **2015**, *10*, 382.
- [34] F. J. O'Brien, B. A. Harley, I. V. Yannas, L. J. Gibson, *Biomaterials* **2005**, *26*, 433.
- [35] L. Qian, W. M. Saltzman, *Biomaterials* **2004**, *25*, 1331.
- [36] Y. Fu, D. Zeng, J. Chao, Y. Jin, Z. Zhang, H. Liu, D. Li, H. Ma, Q. Huang, K. V. Gothelf, *J. Am. Chem. Soc.* **2013**, *135*, 696.
- [37] D. W. Yee, M. D. Schulz, R. H. Grubbs, J. R. Greer, *Adv. Mater.* **2017**, *29*, 1605293.
- [38] P. Wang, T. A. Meyer, V. Pan, P. K. Dutta, Y. Ke, *Chem* **2017**, *2*, 359.
- [39] D. C. Bell, M. C. Lemme, L. A. Stern, J. R. Williams, C. M. Marcus, *Nanotechnology* **2009**, *20*, 455301.